



AFRL-AFOSR-VA-TR-2017-0101

Hybrid Integrated Si/SiN Platforms for Wideband Optical Processing

Ali Adibi
GEORGIA TECH RESEARCH CORPORATION
505 10TH ST NW
ATLANTA, GA 30318-5775

05/08/2017
Final Report

DISTRIBUTION A: Distribution approved for public release.

Air Force Research Laboratory
AF Office Of Scientific Research (AFOSR)/RTA1

REPORT DOCUMENTATION PAGE					Form Approved OMB No. 0704-0188	
<p>The public reporting burden for this collection of information is estimated to average 1 hour per response, including the time for reviewing instructions, searching existing data sources, gathering and maintaining the data needed, and completing and reviewing the collection of information. Send comments regarding this burden estimate or any other aspect of this collection of information, including suggestions for reducing the burden, to Department of Defense, Executive Services, Directorate (0704-0188). Respondents should be aware that notwithstanding any other provision of law, no person shall be subject to any penalty for failing to comply with a collection of information if it does not display a currently valid OMB control number.</p> <p>PLEASE DO NOT RETURN YOUR FORM TO THE ABOVE ORGANIZATION.</p>						
1. REPORT DATE (DD-MM-YYYY) 08-05-2017		2. REPORT TYPE Final Performance		3. DATES COVERED (From - To) 01 Mar 2013 to 31 May 2016		
4. TITLE AND SUBTITLE Hybrid Integrated Si/SiN Platforms for Wideband Optical Processing				5a. CONTRACT NUMBER		
				5b. GRANT NUMBER FA9550-13-1-0032		
				5c. PROGRAM ELEMENT NUMBER 61102F		
6. AUTHOR(S) Ali Adibi				5d. PROJECT NUMBER		
				5e. TASK NUMBER		
				5f. WORK UNIT NUMBER		
7. PERFORMING ORGANIZATION NAME(S) AND ADDRESS(ES) GEORGIA TECH RESEARCH CORPORATION 505 10TH ST NW ATLANTA, GA 30318-5775 US				8. PERFORMING ORGANIZATION REPORT NUMBER		
9. SPONSORING/MONITORING AGENCY NAME(S) AND ADDRESS(ES) AF Office of Scientific Research 875 N. Randolph St. Room 3112 Arlington, VA 22203				10. SPONSOR/MONITOR'S ACRONYM(S) AFRL/AFOSR RTA1		
				11. SPONSOR/MONITOR'S REPORT NUMBER(S) AFRL-AFOSR-VA-TR-2017-0101		
12. DISTRIBUTION/AVAILABILITY STATEMENT A DISTRIBUTION UNLIMITED: PB Public Release						
13. SUPPLEMENTARY NOTES						
14. ABSTRACT This AFOSR-supported research was started in March 2013 and was directed toward developing an integrated photonic platform for wideband, compact, low-power and high-speed coherent optical processing. The envisioned platform will provide different essential functionalities for wideband coherent optical processing (WCOP), such as optical comb sources, modulators, arbitrary signal generation, and linear coherent signal processing. This research was focused on addressing the key fundamental limitations for the deployment of coherent optical processing systems, at all levels, e.g., material platform, device technology, and system design and implementation.						
15. SUBJECT TERMS hybrid integration, integrated photonics						
16. SECURITY CLASSIFICATION OF:			17. LIMITATION OF ABSTRACT UU	18. NUMBER OF PAGES	19a. NAME OF RESPONSIBLE PERSON POMRENKE, GERNOT	
a. REPORT Unclassified	b. ABSTRACT Unclassified	c. THIS PAGE Unclassified			19b. TELEPHONE NUMBER (Include area code) 703-696-8426	

**Final Report to the
Air Force Office of Scientific Research (AFOSR)**

Hybrid Integrated Si/SiN Platforms for Wideband Optical Processing

Georgia Institute of Technology

Principal Investigator:

Ali Adibi

Professor, School of Electrical and Computer Engineering,

Georgia Institute of Technology

Atlanta, GA 30332-0250

e-mail: adibi@ee.gatech.edu

Tel: (404) 385-2738

Fax: (404) 894-4641

Nov. 2016

I. Introduction

This final report summarizes achievements in Dr. Adibi's research group at Georgia Institute of Technology in the area of hybrid integrated material platforms for wideband coherent optical processing, supported by grant number FA9550-13-1-0032. Major achievements during this program (March 1, 2013 to May 30, 2016) with brief descriptions are listed in this report. Detailed information can be found in the recent publications or can be directly requested from Dr. Adibi.

This AFOSR-supported research was started in March 2013 and was directed toward developing an integrated photonic platform for wideband, compact, low-power and high-speed coherent optical processing. The envisioned platform will provide different essential functionalities for wideband coherent optical processing (WCOP), such as optical comb sources, modulators, arbitrary signal generation, and linear coherent signal processing. This research was focused on addressing the key fundamental limitations for the deployment of coherent optical processing systems, at all levels, e.g., material platform, device technology, and system design and implementation.

During this program, we have focused several important tasks including 1) development of a new high-quality hybrid material platform based on three-dimensional (3D) integration of different material layers, 2) demonstration of different integrated photonic devices based on the multi-layer material platform, 3) development of different techniques for the high-efficiency light coupling between different material layers, and 5) modeling, simulation, and design of nonlinear devices for stable and wideband coherent comb generation and ultrafast pulse generation in this material platform. Our research during this program has resulted in several important accomplishments that have been (are being) reported through journal publications and conference presentations. Specifically, we have: 1) developed and optimized new multi-layer material platforms including double-layer-silicon(Si) and hybrid multi-layer Si/silicon nitride (SiN) material platforms with the best material qualities reported to-date as evidenced by the performance of the fabricated devices, 2) developed mechanisms for high-efficiency coupling of light between different Si and SiN layers in the hybrid Si/SiN material platform, 3) developed novel integrated photonic modulators in the hybrid Si/SiO₂/Si and Si/SiN material platforms with unique performance measures without any power-consuming trimming mechanism, 4) demonstrated the concept of optical bistability in photonic crystal resonators on chip, 5) developed wideband tunable opto-mechanical devices and showed the possibility of achieving stimulated Brillouin scattering (SBS) in optomechanical structures on chip, and 6) demonstrated an effective technique for wideband comb-generation and soliton formation using input phase modulation. This report covers some of the accomplishments through this program. More information can be found at the previous annual reports as well as the published journal and conference papers listed at the end of this report.

II. Research Accomplishments

In this section we briefly review the main results and accomplishments during in this program in different areas. More details can be found in the recent publications or will be available upon request.

II.A Development of high-quality multi-layer material platform

Conventional integrated nanophotonic structures are primarily formed on silicon-on-insulator (SOI) substrates [1]. Si has been by far the most highly used material due to its unique electro-optical characteristics such as high refractive index, relatively low optical loss while electrically semiconductive, as well as its compatibility with standard CMOS fabrication processes, has made silicon (Si) a suitable choice for planar lightwave circuits. However, the absorption mechanisms, such as two-photon and free-carrier absorption, limit the capacity of silicon to handle high optical powers or support ultra-low-loss optical elements. Among the alternatives for high power/low loss operation, silicon nitride (SiN) has recently gained a lot of attention (due to its very low loss and small nonlinearity) as a promising, CMOS-compatible material platform for integrated photonic applications [2]. Especially, stoichiometric SiN deposited using low-pressure chemical vapor deposition (LPCVD) offers very low intrinsic optical loss and superior reproducibility. Recent studies have demonstrated an order of magnitude lower optical loss in SiN compared to Si [3]. However, the dielectric nature of SiN hinders its use for active (e.g., electro-optical) devices such as modulators. While neither Si nor SiN seems to have all the properties needed for next generation integrated nanophotonic platforms, a hybrid multi-layer material system can combine their unique capabilities to provide a solution to this challenge. Such a multi-layer structure can be extended to have more functionalities (e.g., strong nonlinearity, very fast carrier dynamics, etc.) by adding more layers of other CMOS-compatible functional materials (e.g., polymers, graphene, planar materials, etc.). The key requirement is to have high-quality low-loss materials in different layers (e.g., through highly optimized bonding or deposition processes).

In this program, we have developed alternative multi-layer material platforms based on heterogeneous stacking of different material layers to achieve new functional devices that cannot be achieved in single layer SOI material platform. We have specifically developed multi-layer Si substrates that allow for new higher efficiency devices based on capacitive devices (e.g., accumulation-based modulator and widely tunable mechanical resonators) and hybrid material platforms based on vertical integration of Si with silicon nitride (SiN), graphene and other two-dimensional materials.

To benefit from key features of different CMOS-compatible materials on a single chip, creating a During the first phase of this program on hetero-material structures, we have developed optimal processes for forming a series of hybrid multi-layer materials for integrated nanophotonics, including double-layer Si (Si/SiO₂/Si as the device material) and hybrid Si/SiO₂/SiN.

II.A.1 Development of high-Q multi-layer Si material platform: We demonstrated the viability of achieving high optical-quality double-layer Si material platform by bonding two SOI wafers and fabricating and characterizing basic waveguide and resonator devices. Figure 1(a) shows the scanning electron micrograph (SEM) of the cross-section of a double-layer Si waveguide. Figure 1(b) shows the transmission spectrum of one of the TE-polarized resonances of a 20 μm radius microdisk with an intrinsic quality factor (Q) of 500K, which is by far the highest achieved to date

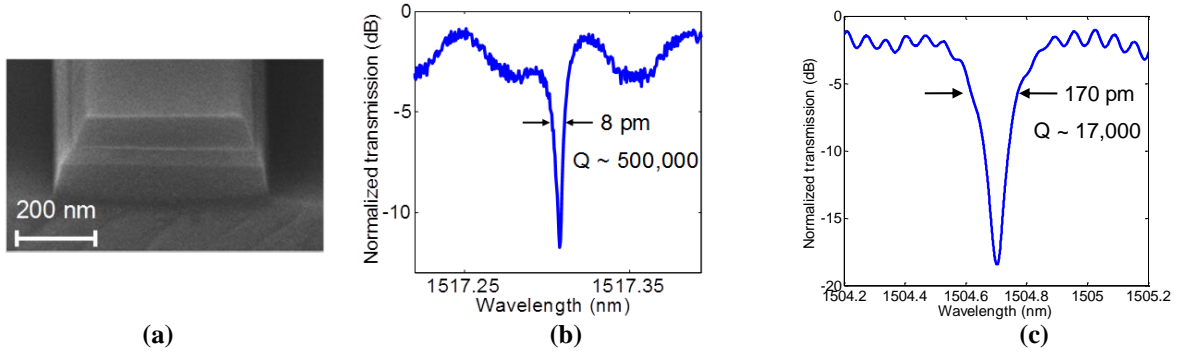


Figure 1. (a) SEM image of the cross-section of a double-layer Si waveguide in which each of the two Si layers are 110 nm and the interface oxide is 60 nm thick. (b) and (c) show the transmission spectra of one of the TE-polarized resonances of a 20 μm and 2 μm radius microdisk resonator, respectively.

in any double-layer Si structure. Figure 1(c) shows the transmission spectrum of one of the TE-polarized resonances of a 2 μm radius microdisk with intrinsic Q of 17K. This is the most compact high-Q resonator ever developed on a double-layer Si platform. The proposed multi-layer double layer SOI material provides a flexible platform for demonstration of functional photonic and optoelectronic material platforms. In this program, we have used this material platform to develop high quality modulators and switches based on carrier accumulation by applying voltage between the upper and lower electrodes in a resonator structure. Furthermore, this material platform can be used to demonstrate functional photonic structures by undercutting the middle SiO_2 layer and infiltration of the gap between the two layers with organic or inorganic materials using polymer infiltration or the atomic layer deposition (ALD) process. We have already developed a reliable process for undercutting the oxide layer between the two Si layers in this material platform (see Figure 2(a)) for infiltration with either high-k dielectrics using ALD (see Figure 2(b)) or polymers.

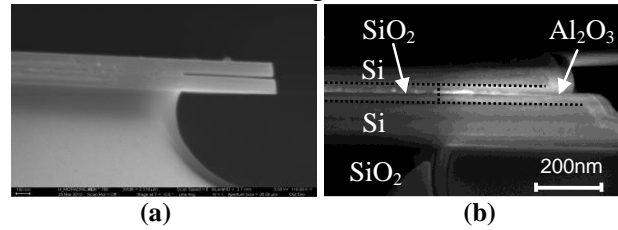


Figure 2. (a) A microdisk resonator fabricated in the double-layer Si platform with undercut SiO_2 layer; (b) partial undercutting of the SiO_2 layer and its replacement with Al_2O_3 using ALD in a double-layer Si material platform.

II.A.2. Development of compact, low-loss and high-bandwidth devices in Si/SiN hybrid platform: We have developed two alternative approaches for development of hybrid Si/SiN material platform based on 1)

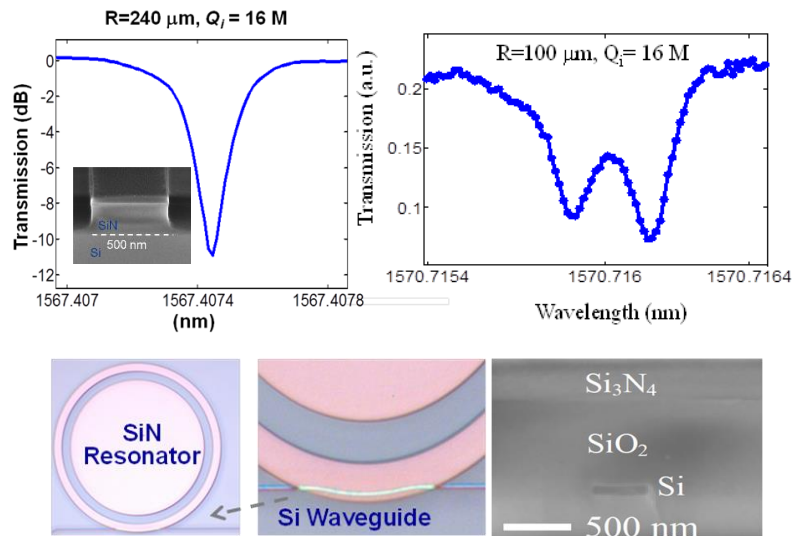


Figure 3. (top) Transmission spectrum through the Si waveguide demonstrating a Q of 16M for a SiN microdisk with 240 μm (left) and 100 μm (right) radii (Inset shows the resonators cross-section). (Bottom) Fabricated SiN resonator on the hybrid SiN/SOI material platform and its cross-section

vertical integration of SiN on top of Si based on layer-by-layer material deposition and device fabrication [4,5], and 2) back-end integration of SiN and Si based on wafer bonding and layer transfer [6].

We have previously demonstrated the possibility of development of high-quality SiN film using low-pressure chemical vapor deposition (LPCVD) and developing high quality SiN resonators with Qs up to 16 M (Figure 3). We have also demonstrated hybrid Si/SiN material platform based on the LPCVD deposition of SiN on the SOI platform and demonstrated hybrid devices based on efficient coupling of Si-based waveguides on the SOI platform to SiN resonators. While this approach is effective for some applications, the need for high-temperature for LPCVD SiN deposition and annealing process, makes the process prone to dopant redistribution, that hinders the SiN deposition after full Si device fabrication. To resolve this issue, we developed a new techniques for fabrication of the hybrid Si/SiN material platform based on a high-quality wafer bonding process (Figure 4). The main advantage of this new process based on wafer bonding is the possibility of wafer-scale development of Si/SiN material platform that allows for deposition of even higher-quality SiN films. To achieve the high quality hybrid SiN/SOI material platform along with a good fabrication yield, we have carefully optimized the condition for SiN deposition as well as the bonding process. By appropriate management of SiN film stress, we are now able to develop SiN films with thicknesses up to 1000 nm and developed reliable bonding process with close to 100% yield.

The fabrication process for the integration of silicon onto SiN is schematically summarized in Figure 5. We start with growing 30 nm of thermal SiO₂ on top of a SOI die with 220 nm of crystalline Si. In parallel, a Si die goes through a wet oxidation process to grow 5 μ m of thermal oxide. In the next step, 400 nm of LPCVD SiN is deposited with dichlorosilane (DCS) and ammonia (NH₃) precursors using 1:3 gas ratio. Then a 30 nm layer of SiO₂ is deposited on top of the SiN using atomic layer deposition (ALD). The choice of deposition method is made by

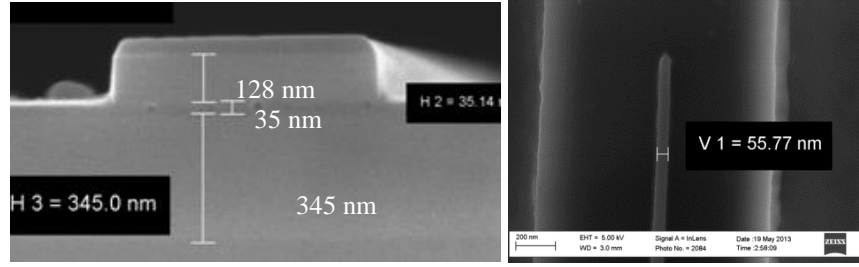


Figure 4. Cross-section (left) and top-image (right) SEM images of a waveguide fabricated on the hybrid SiN/SOI material platform based on bonding of SOI wafers on LPCVD SiN with a buffer SiO₂ layer.

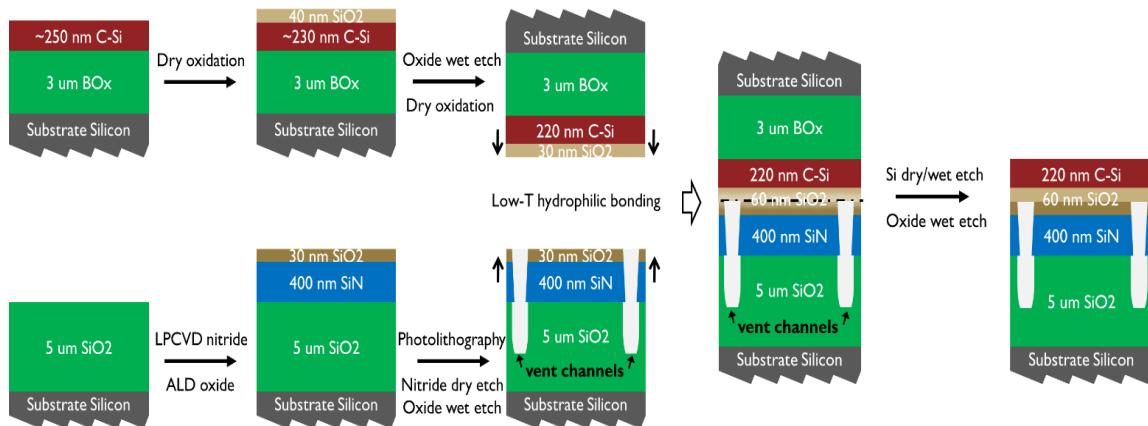


Figure 5. The fabrication process for the development of hybrid Si on SiN platform based on hydrophilic oxide bonding

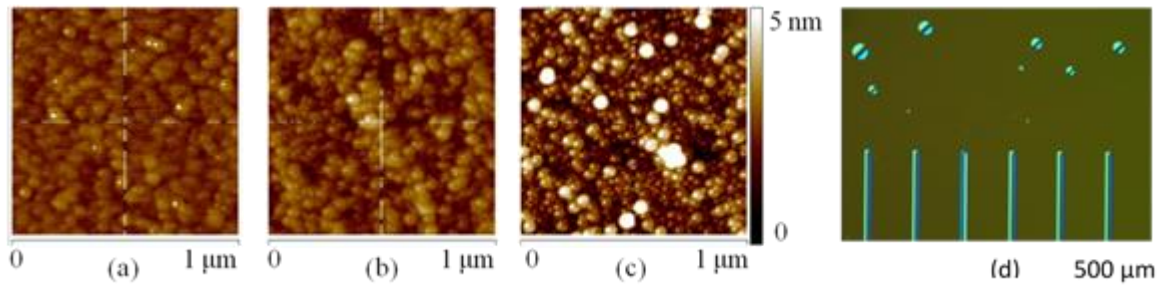


Figure 6. AFM images from the surface of 40 nm SiO_2 layer deposited by (a) HSQ annealing, average surface roughness (R_a) is 2.39 Å; (b) ALD, $R_a = 3.83$ Å; (c) PECVD, $R_a = 7.45$ Å; (d) a bonded sample at the edges where the vent channels are terminated. Bubbles can be clearly seen in the area without vent channels.

comparing plasma-enhanced chemical vapor deposition (PECVD), ALD, and hydrogen silsesquioxane (HSQ) annealing methods. As a figure of merit in hydrophilic bonding, we monitored the surface roughness and bonding strength of a thin oxide layer to the SiN layer. Figures 6-a to 6-c show the roughness measurement of each material deposition method using atomic force microscopy (AFM), in which HSQ annealing and ALD provide considerably better quality than PECVD. The bonding strength is characterized by running separate bonding tests for HSQ annealing and ALD methods. We measured the blade crack-opening depth from the facet of the bonded die after bonding a pair of dies of the same material interface. Lowest average crack-opening depth is measured for ALD ($D < 1$ mm) and HSQ ($D = 2.1$ mm). Since the bonding strength contrast is more pronounced than roughness between the two methods, ALD is chosen for oxide deposition. In the next step, the die goes through a set of wet and dry etching processes to carve out channels of 10 μm width with 250 μm spacing from each other. As shown in Figure 1-d, by adding these "vent channels" into the die, the trapped air and chemical by-products of bonding can escape the interface, resulting in the void-free fusion of the two dies. Details of the bonding process is described in our previous work on DLSi platform [7].

In order to test the full functionality of the platform, a hybrid optical path is envisioned and implemented on the hybrid platform (Figure 7). The characterization results

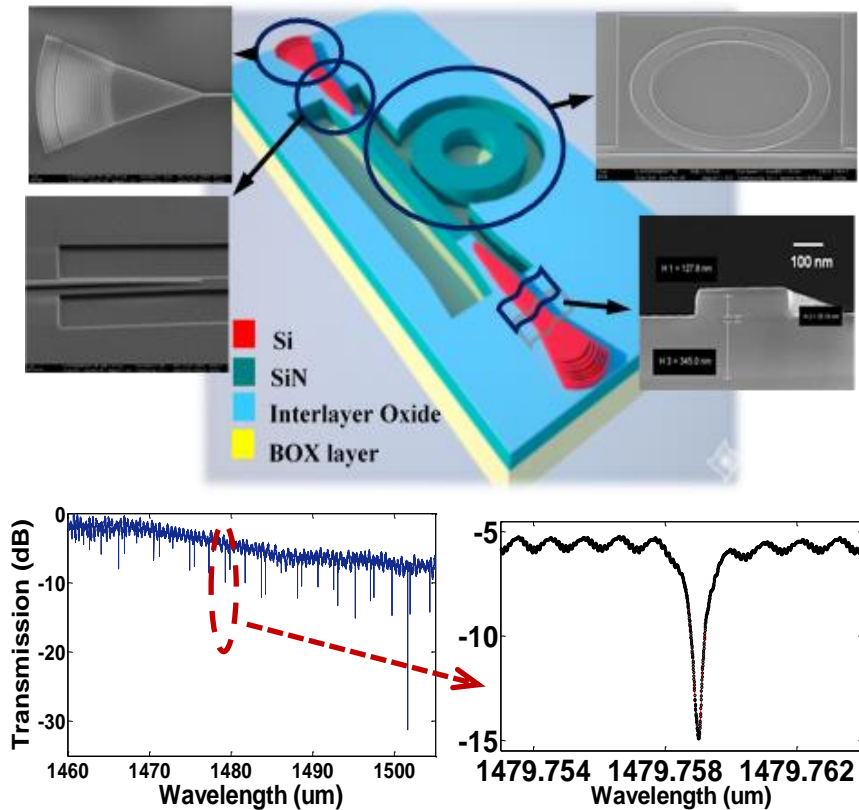


Figure 7. The schematic of hybrid optical path; the inset includes SEM images of building blocks of the path and the characterization readout of the transmission spectrum.

show average quality factor (Q) for SiN micodisk resonators of $40\text{ }\mu\text{m}$ radius to be $Q_{\text{int}} = 3 \times 10^6$ in the hybrid platform (Figure 7 inset), which is the same as the average Q of the SiN resonators fabricated on an inspection SiN on SiO₂ die in parallel to the bonded die. To the best of our knowledge, this is the highest Q reported to date for a hybrid SiN/Si resonator of this compact size. It also indicates that the bonding process does not increase the optical loss. In order to measure the insertion loss of the couplers, a set of 8 pairs of couplers are cascaded, and the output optical signal is measured.

II.B Coupling between different material layers in multi-layer material platforms

The formation of functional integrated photonic systems using our developed hybrid material platform requires efficient coupling of light between different layers as coupling losses can add up to a large overall insertion loss. We have developed two techniques for achieving such efficient coupling in the hybrid material platform based on high efficiency grating coupling and evanescent tapered coupling. The first approach provides a technique for coupling between different with relatively large vertical separation and is independent of the separation layer thickness, the second approach provides a very-low-loss coupling between evanescently coupled material layers.

II.B.1 Optimized inter-layer grating couplers: Figure 8(a) shows the schematic of the proposed coupling structure in a 3D Si/SiO₂/SiN hybrid material platform. In this structure light from a ridge waveguide in the (lower) Si device layer is coupled to a SiN microring resonator in the higher layer through a SiN waveguide. The coupling between the two layers is achieved by using two gratings in the Si and SiN layers (see Figure 8(b)). These two layers are separated by a relatively thick SiO₂ buffer layer to minimize the unwanted crosstalk coupling between the layers.

To design and optimize the interlayer grating couplers in Figure 8(b), several design parameters can be chosen. While the thicknesses of these layers (i.e., Si, SiO₂, and SiN) can be considered as design parameters, they are usually selected by practical considerations. For example, commercially available SOI wafers offer only a few options for the thicknesses of the SiO₂ buried oxide (BOX) and the Si device layers, respectively, to comply with practical requirements. The thickness of SiN layer is 400 nm. The top cladding layer (SiO₂) thickness is chosen to be $2.25\text{ }\mu\text{m}$. We also assume fixed etch depths of 90 nm and 400 nm for the gratings on the Si and SiN layers, respectively, during the optimization. As shown in Figure 8(a), the top of the cladding and bottom of the BOX layers are also coated with a thin reflective metal to enhance the efficiency of the power transfer in a vertical Fabry-Perot cavity, on the two sides of the interlayer grating coupler.

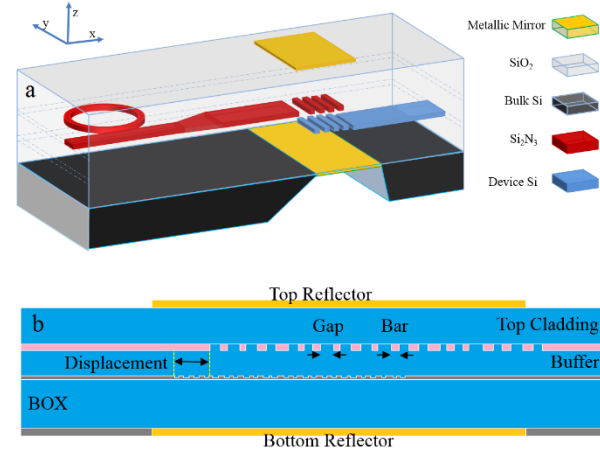


Figure 8. (a) Schematic of the interlayer grating coupler enhanced with top and backside metallic reflectors to couple light from a Si waveguide (lower layer) to a ring resonator coupled to the access waveguide on the SiN layer (top layer). (b) Detailed cross section of the device around interlayer grating coupler. Each grating period is divided into a material (i.e., Si or SiN) part (called “bar”) and a groove part (called “gap”). The beginning of the top layer grating is displaced from that of the bottom layer grating by an amount called “displacement”. The gratings on the Si and SiN layers contain 18 and 24 grooves, respectively; and their widths and positions are found by the optimization process.

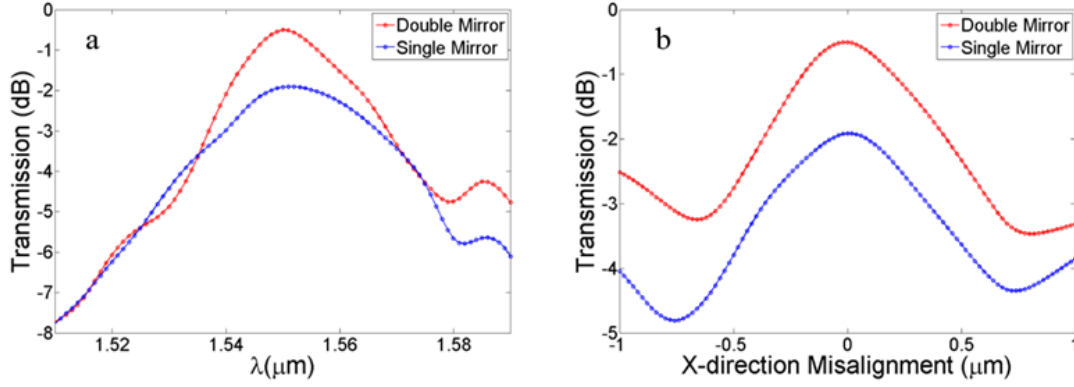


Figure 9. (a) Calculated frequency response of the optimized interlayer grating coupler with single/double metallic mirrors obtained through FEM simulations; (b) Effect of X-direction misalignment of the SiN grating on the insertion loss for the optimized single/double-mirror grating couplers.

With layer thicknesses fixed, the problem of designing the efficient interlayer coupler reduces to finding optimal geometries for the two gratings in the Si and SiN layers. In this optimization, we assume the bottom (Si) and top (SiN) gratings to have 24 and 18 grooves (periods), respectively. The design parameters are the groove width (identified by "gap" in Figure 8(b)) and the material width (identified by "bar" in Figure 8(b)) in each period of each grating. This is an unconstrained global optimization problem with the reward function being the coupling efficiency. Considering the high-dimensional search space (assuming the grating geometries are arbitrary), brute-force search approaches are not feasible due to the extremely high computational cost. Metaheuristic approaches such as genetic algorithm (GA) or particle swarm optimization (PSO) are highly effective in dealing with different classes of optimization problems. In our case, we developed a GA code (in Matlab) to perform geometrical optimization.

We optimized two grating architectures based on single (top) and double (top and bottom) reflectors using the developed FEM analysis and GA optimization approach. Figure 9 shows the simulated coupling efficiency of these structures as well as their sensitivity to misalignment between the patterns on Si and SiN layers. Peak coupling efficiencies of 89% (double-mirror) and 64% (single-mirror) for excitation wavelength of 1550 nm with about 40 nm bandwidth is achieved with low sensitivity to misalignment errors.

Figure 10 shows the schematic (optical image and SEM) of the fabricated device as well as the simulated field profile of the device at the grating region. Figure 10 (down) shows the transmission of the device with a single metallic mirror on top of the device. It is clear from Figure 10 that coupling efficiency better than 2 dB is achieved, which is close to the simulation results (64%).

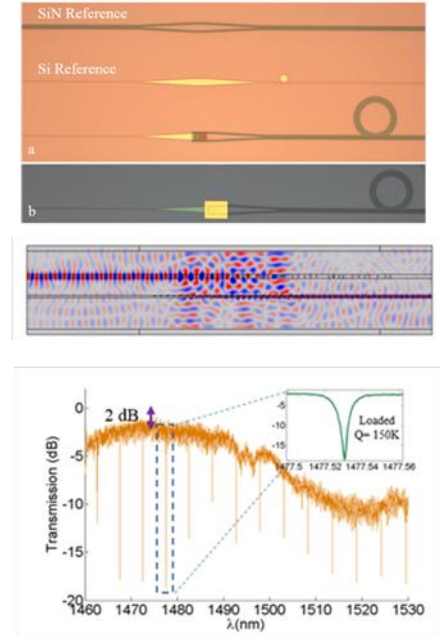


Figure 10. Coupling a Si waveguide (lower layer) to a SiN waveguide (higher layer) that is coupled to a ring resonator: (top) optical image and SEM image (middle) the simulated field pattern of the grating coupler between two layers, (down) Transmission spectrum of the device showing coupling efficiency better than 2dB.

II.B.2 Very low-loss inter-layer couplers based on tapered evanescent couplers:

The design of hybrid Si/SiN devices, requires very low-loss approaches to route the light between different material layers. Therefore, to achieve low-loss interlayer couplers, we have designed evanescent couplers with linearly tapered Si and SiN couplers. In our design, the Si waveguide is tapered down to 50 nm width in 30 μm length, while the underneath SiN blanket is also tapered down to 1 μm final width. Finite different time domain (FDTD) simulations of a 30 μm hybrid coupler (Figure 11) show a superior broadband

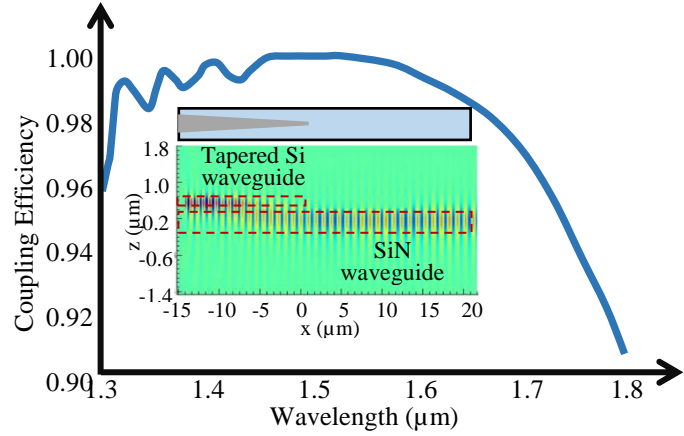


Figure 11. Coupling efficiency vs. wavelength between Si and SiN layers in hybrid Si/SiO₂/SiN material using tapered coupling. Inset shows the field profile in the tapered area simulated using the finite difference time domain (FDTD).

coupling efficiency, close to 100% for more than 500 nm 3-dB bandwidth. Figure 12(a) shows the fabricated coupler structure. To characterize the optical loss of the evanescent tapered couplers several arrays of 16 and 32 cascaded couplers between silicon and SiN are fabricated and characterized. The measured optical loss is determined to be as low as 0.02 dB/transition for 30 μm coupler, as shown in Figure 12(b), which is a record low to the best of our knowledge. It can be shown that such low-loss interlayer transitions owes itself to the ultra-thin interface SiO₂ layer of 60-70 nm thickness and the hybrid tapering method, in contrast to inverse tapering scheme which leads to comparatively higher losses.

II.C Demonstration of high-speed modulators based on hybrid material platform

II.C.1 High-speed accumulation-based electro-optic modulator: Carrier dispersion offers a fast way to change the optical properties of Si, in particular its refractive index and optical absorption. Carrier injection and depletion in a pn-junction device and carrier accumulation in a capacitive device are the main mechanisms by which the carrier concentration in Si can be altered. In contrast to the injection mechanism in which the lifetime (τ_c) of the excess (minority) carriers limits the speed of the process, the relaxation time of the electrical circuit ($\tau = RC$) plays the deciding role in the charge dynamics in cases of depletion and accumulation mechanisms. Since it is rather easy to engineer the RC of the device such that $\tau \ll \tau_c$, most of the current studies for high-speed electro-optic modulation applications are focused on the depletion mechanism in devices with a reverse-

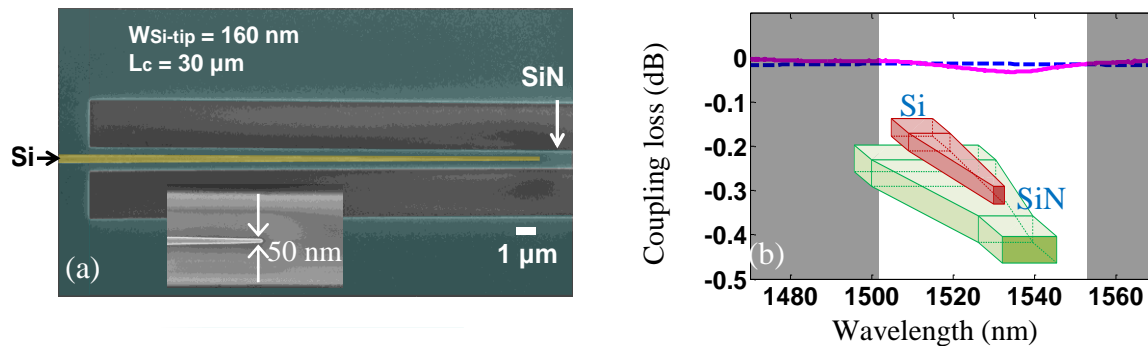


Figure 12. Low-loss coupling between waveguides in Si and SiN material layers. (right) SEM picture of the fabricated coupler, (left) measured coupling loss for a coupler with 30 μm length based on a cascaded array of couplers.

biased pn-junction. In a typical reverse-biased pn-based modulator the capacitance (C) and resistance (R) of the device are mainly decided by the doping levels (N) on the p and n regions such that RC is proportional to $N^{-1/2}$. In practical cases the doping levels in such structure are kept as low as $1\text{-}2 \times 10^{18} \text{ cm}^{-3}$ due to the loss associated with the dopants. In comparison to depletion mechanism, carrier accumulation is less explored. High-speed electro-optic modulation based on accumulation mechanism has been studied and demonstrated in resonance- and interferometric-based architecture featuring an embedded MOS capacitor.

In such structures a doped poly Si layer is used as the top gate electrode and a crystalline Si layer serves as the second electrode. In general, due to scattering from the grain boundaries, use of poly Si significantly affects the performance of integrated optical devices and hence is not desirable. Most notably the scattering loss degrades the quality factor (Q) of compact resonance-based devices. In this work we demonstrate the use of a multilayer platform which allows us to achieve a high-speed electro-optic modulator in a compact and low-loss microdisk featuring crystalline Si layers for both capacitor electrodes.

The cross section schematic of the electro-optic modulator is shown in Figure 13 (a). The device comprises a microdisk ($3\mu\text{m}$ radius) optical resonator and a 450 nm wide access waveguide which are fabricated on a multilayer Si/SiO₂/Si platform. The thickness of the top and bottom Si layers is 110 nm each and the middle SiO₂ layer is 60 nm thick. The access waveguide is placed 150 nm away from the microdisk to achieve near critical coupling through evanescent excitation. A 50 nm thick Si pedestal underneath the device provides access to the bottom Si layer. The top and bottom Si layers are doped to reduce their electrical resistivity. The cross section of the doping profile on the microdisk is shown in Figure 13 (b). The electrodes are deliberately placed far from the first radial whispering gallery mode of the microdisk to ensure negligible propagation loss due to metallization (See Figures 13 (b) and (c)). The optical field profile of the first radial mode of the microdisk is shown in Figure 13 (c). This device is fabricated on our bonded Si/SiO₂/Si multilayer platform using standard nanofabrication techniques. Figure 14 (a) shows the scanning electron microscope (SEM) image of the waveguide and part of the microdisk (tilt angle is 45°) before metallization and cladding steps. The blue and pink shaded regions correspond to the Si and oxide layers, respectively. Figure 14 (b) is the top view SEM image of the overall device after cladding and metallization steps.

To characterize the device, the chip is mounted on a thermally controlled stage and fixed using a conductive double sided adhesive tape. Two flat-cleaved single mode fibers (SMF) were used to couple light in and out of the chip through the grating couplers. SMF fibers were mounted on a stage equipped with manual xyz translation as well as tilt and rotation adjustments. We use a tunable laser source (Agilent 8164A) to feed the input SMF fiber. In order to adjust the state of polarization of the light impinging upon the input

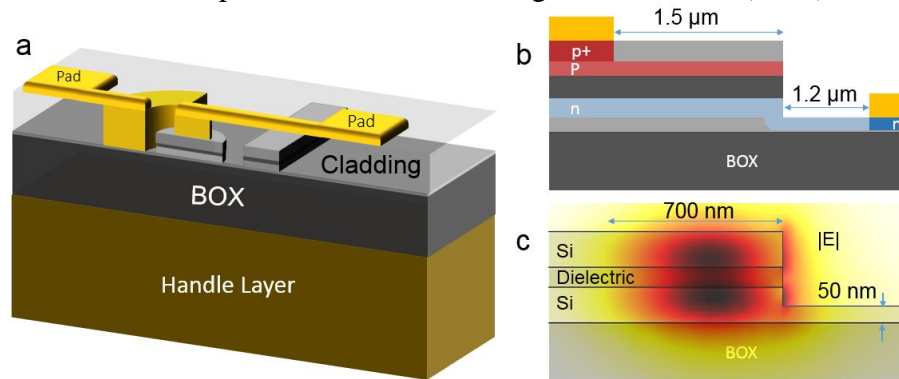


Figure 13. (a) 3D schematic of the cross section of the accumulation-based electro-optic modulator on a multilayer platform. (b) Cross section view of the designed doping profile on different layers of the device. (c) The corresponding mode profile (magnitude of the electric field) of the first radial mode of the microdisk around 1550 nm computed by FEM software package (COMSOL).

grating coupler, a 3-paddle polarization rotator is strung on the input fiber. The optical power of the collected signal at the output is boosted through an Erbium-doped fiber amplifier (EDFA) module with a total fixed gain of 21dB. The optical amplification has

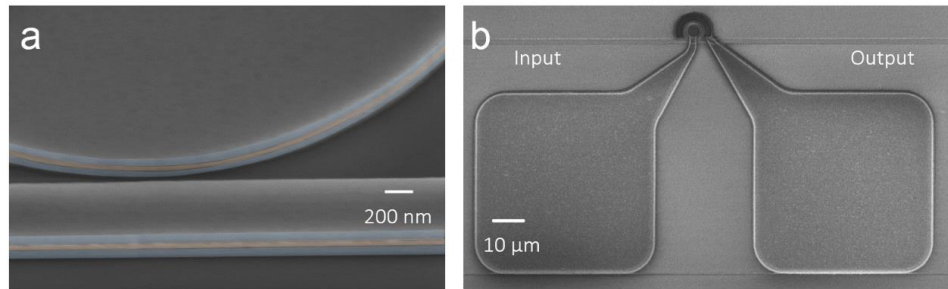


Figure 14. (a) Tilted SEM image of the gap region between the access waveguide and the microdisk. False colors are used to accentuate the stacked Si and oxide layers (b) Top view SEM image of the device after metallization showing the input/output waveguide, microdisk and RF electronic pads. Pads are placed close to the microdisk (<50 μm) to prevent long transmission lines effect.

been carried out to make the detector thermal noise small compared to the signal. However, in order to avoid the nonlinear response from the photoreceiver a variable optical attenuator (Agilent 8156A) is placed right after the EDFA to fine tune the optical power in the feeding output fiber. To detect and correct for any drift in the fiber/grating alignments during the experiment, the received optical power was constantly monitored by tapping a small portion of the signal using a 10/90 directional coupler. The aggregate physical length of the output fiber from the modulator to the photoreceiver (apart from the EDFA) is approximately 10 meters. A high speed (i.e., cutoff frequency of 35GHz) photoreceiver (PT-40G from Advanced Photonix Inc.) is used at the receiving end of the circuit. The output voltage of the photoreceiver is monitored both in time domain and frequency domain using a wide bandwidth oscilloscope (DCA-X 86100D) and an electrical spectrum analyzer (Agilent 8564EC). Figure 15 is the measured frequency response of the electro-optic modulator clearly shows an upper 3-dB cutoff frequency of more than 10 GHz. The inset image shows the eye-diagram of the measured photodetector voltage while the modulator is driven by a sine wave at 10 GHz.

II.C.2 Design and fabrication of high-speed, high-quality resonant coupling modulation in the SON hybrid material platform: Among various integrated photonic components, microdisk and microring resonators have been the focus of substantial research to produce low-power, high-speed, and compact integrated modulators [8,9]. Such modulators are extensively used in different chip-scale applications, including on-chip interconnection, photonic analog-to-digital conversion, and optical pulse-shaping [10]. The main figures of merit for modulators are high speed, high energy efficiency, low insertion-loss, high extinction ratio, and compact size. Such performance metrics

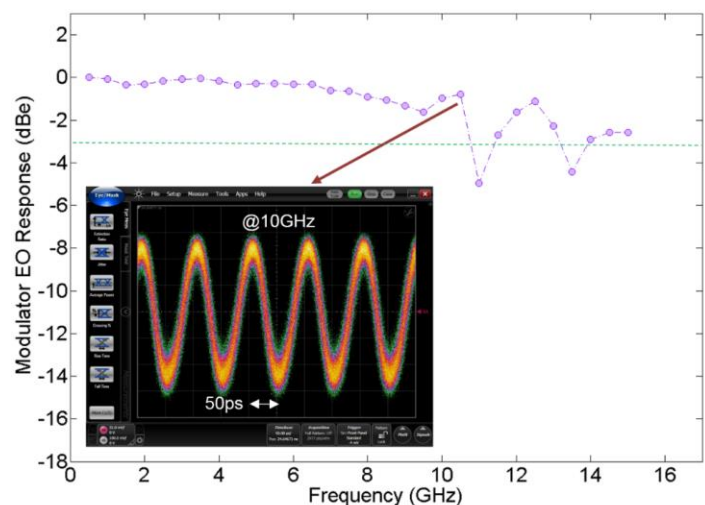


Figure 15. The measured frequency response of the electro-optic modulator clearly shows an upper 3-dB cutoff frequency of more than 10 GHz. The inset image shows the eye-diagram of the measured photodetector voltage (modulator is driven by a sine wave at 10 GHz).

can be significantly improved using amplified coherent light in resonance-based structures. In principle, microrings with higher Q's can offer higher electro-optical conversion sensitivity and improve all the corresponding metrics. However, there is a fundamental trade-off between the speed of modulation and the cavity lifetime in the majority of resonant-modulation methods. Therefore, the power-efficiency and speed cannot simultaneously increase in such designs.

Recently, there has been an increasing attention toward integrated devices based on coupling modulation [11,12]. Such devices share a common modality in which the fundamental limit of speed against cavity lifetime is removed, enabling a set of promising devices for switching, amplification, and modulation. However, the efficient performance of the coupling modulation critically depends on the finesse of the optical cavity. Figure 16(a) shows the schematic of a typical coupling modulator design. As illustrated in Figure 16(b), for a given resonator, the Q factor is directly proportional to the slope of change in the power transmission. Therefore, a higher Q cavity utilizes a higher optical output swing for a fixed coupling swing.

To understand the dynamics of modulation, a universal solution of the configuration in the Figure 16(a) is needed. The transfer matrix method is used to find the transmission at each point of time through a recursive formula. Then the method of successive substitution solves such relation to find the transmission function, i. e. $T(t)$, as following,

$$(1) \quad T(t) = e^{-j\theta} \left[\tau(t) - \alpha \frac{\kappa(t)}{\kappa(t-t_0)} \right] + e^{-j\theta} \kappa(t) \sum_m \left(\alpha^m \left[\frac{\tau(t-mt_0)}{\kappa(t-mt_0)} - \frac{\alpha}{\kappa(t-(m+1)t_0)} \right] \prod_{p=1}^m \tau^*(t-pt_0) \right),$$

in which, $\alpha = ae^{-j(\theta+\phi)}$, and a is the attenuation associated with a roundtrip (of time constant t_0) inside the resonator, and ϕ is the propagation phase shift of the roundtrip, and θ is the coupling phase shift. For small signal response of transmission in the high-Q regime of the cavity, and for frequencies that are smaller than $1/t_0$, the Eq. 1 can be simplified to the following

$$(2) \quad T(t) = e^{-j\theta} \tau(t) - \alpha \kappa(t) \times X_0.$$

In Eq. 2, the X_0 factor is the steady-state electromagnetic field amplitude inside the resonator, which is directly proportional to the field enhancement, and finesse of the cavity. Therefore, as the finesse increases, $\kappa(t)$ is proportionally amplified in the output, which confirms the computed results in Figure 16(b).

Building on the insight provided by the coupling modulation theoretical analysis, we proposed the device design as shown in Figure 17(a). The resonator is realized in SiN as the ultra-low-loss material, and Si offers the reconfigurability for the high-speed modulation. The time-varying coupling coefficient $\kappa(t)$ is realized through two fixed couplers in SiN layer and a pair of interlayer vertical couplers which transfer light from SiN to Si layer. The final piece is a phase shifter arm in Si which can be tuned fast enough to guarantee GHz functionality of the time-varying coupler. Changing the fixed coupler coefficients in SiN, the power can be balanced between different materials to support an overall high-quality device while enabling the high-efficiency of the modulator. The design of our hybrid coupling modulator device is composed of a racetrack SiN resonator with the total perimeter of $\sim 650 \mu\text{m}$, two fixed SiN waveguide-resonator couplers with equal (power) coupling efficiency ($|\kappa|^2$) of 0.133, a pair of ultra-low-loss interlayer couplers, and a Si phase shifter waveguide with an effective length of $250 \mu\text{m}$. Figure 17(b) shows the computed response of the device due to the change in the phase shifter arm. Typically, a phase shift of $\pi/10$ gives an output swing of more than 5 dB. The computed Q of the hybrid Si/SiN resonator is about 100k. The high Q of the hybrid resonator and high coupling coefficient of each coupler results in high sensitivity of the output optical signal to the change of the phase of the Si phase-shifter. Figure 18 shows the micrograph of the fabricated passive device in SON platform.

To confirm the functionality of the modulator device in the passive mode, one idea is to use the large thermo-optic coefficient (TOC) of Si in comparison to SiN. At the room temperature, Si has a TOC of 1.5×10^{-4} RIU/K, while the LPCVD SiN has been measured to have a TOC equal to 2.45×10^{-5} RIU/K [13,14].

The large difference of TOC between two materials enables to change the phase of Si phase-shifter arm by heating the whole sample, which effectively changes the refractive index in Si while the change in SiN is negligible. Figure 19 shows that a small change of the sample temperature (5°C) results in a considerable change in the modulator output spectrum. Such change in the temperature is approximately equal to 0.2π phase shift in the Si arm. From the thermal characterization results, it is clear that by modulating the phase in the Si arm, the extinction of the resonance changes more than 15 dB, which is the signature of coupling modulation.

The optimization of ion implantation dosage and energy of ions for each step is done using the TRIM software. We also optimized a rapid thermal annealing (RTA) process which is suitable for the activation of the specific set of ions in our p-n junction design. In the SON platform, the Si waveguide sits on top of a SiN thin-film blanket. The thermal expansion discrepancy between the two materials can break or peel off the Si waveguide at elevated temperatures, rendering the device dysfunctional after annealing. While temperatures higher than 1050°C is commonly used to activate the implanted ions in crystalline Si, the critical limit of hybrid platform requires to keep the annealing temperature below thermal damage point of the device. An extensive search is done to find the minimum temperature for activation of all ions present in the p-n junction to levels above 50%. The minimum temperature of 850°C is found to be the floor temperature. Then we tested a set of passive devices to study the damage of Si waveguide after 5 minutes of RTA at different temperatures. The maximum compliance temperature, defined as the temperature for which more than 95% of devices are functional after RTA, is experimentally found to be 925°C . Adding a safety margin of 25°C , the actual hybrid modulator is annealed at 900°C for 5 minutes. Finally, the contact pads are

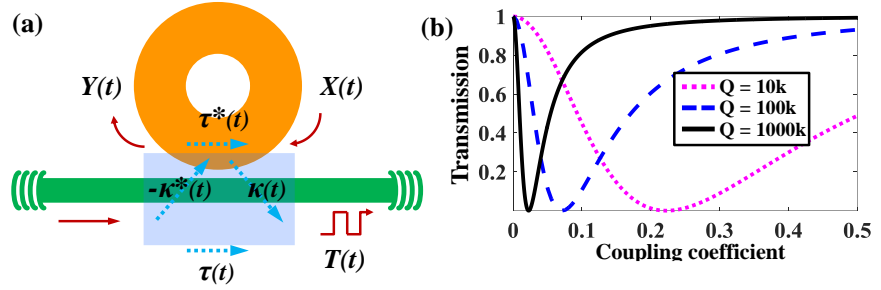


Figure 16. (a) Schematic of a resonant coupling modulation device. $\kappa(t)$ represents the field coupling coefficient from waveguide to resonator. (b) Output power transmission as the function of $|\kappa|$ for three different Q values of a typical integrated resonator. Notice the sharp transition of transmission at low $|\kappa|$ values as Q increases.

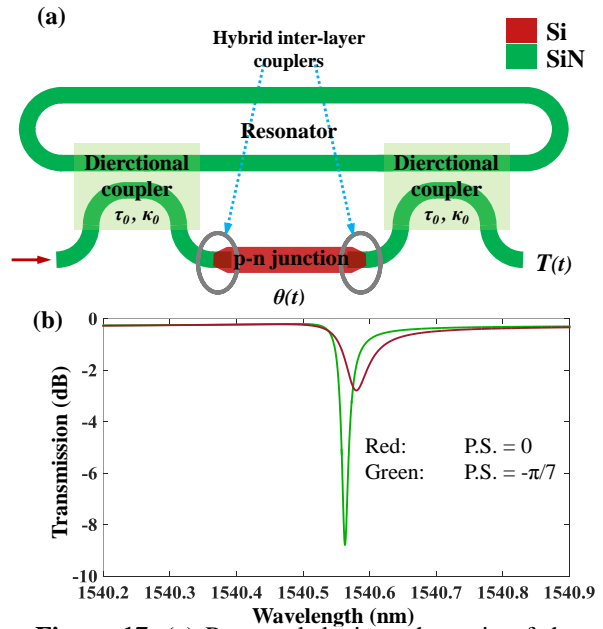


Figure 17. (a) Proposed device schematic of the hybrid coupling modulation device. (b) Output power transmission response of two different phase shifts in the Si waveguide.

incorporated through an aligned EBL, selective dry etching of the ALD oxide in F-based plasma to reach to Si pedestal, followed by an e-beam evaporation of a 500 nm of Au on top of 20 nm buffer layer of Ti, and the final lift-off. Figure 20(a) inset shows the fabricated device with Au pads, and the corresponding i-v curve of the p-n junction realized in Si waveguide as well as the DC electro-optical response of the device are shown in Figure 20(a) and 20(b).

The results of DC i-v characterization of the p-n junction in Si waveguide confirms the functionality of the diode. The three sections of p-n diode can be clearly distinguished in the corresponding i-v curve: 1) the reverse-voltage region with the $I_{\text{rev}} \sim 1\text{-}5\text{ nA}$; 2) the forward bias onset of $\sim 0.5\text{ V}$ with the exponential i-v characteristic of the diode; 3) the resistance limited region with the onset of $\sim 1\text{ V}$. The total resistance of the p-n junction device, including the contacts and pads, is measured to be as low as $19\ \Omega$. The measured result clearly confirms the success of our proposed process to deliver ohmic contacts of ultra-low-resistivity. Considering an active length of $100\ \mu\text{m}$ of this measured device, the total capacitance is equal to $\sim 50\text{ fF}$. Therefore, the 3-dB bandwidth of the device will be $(2\pi RC)^{-1} \sim 160\text{ GHz}$. If the additional $50\ \Omega$ probe resistance is also considered in the total resistance, the 3-dB speed still can be as high as 40 GHz .

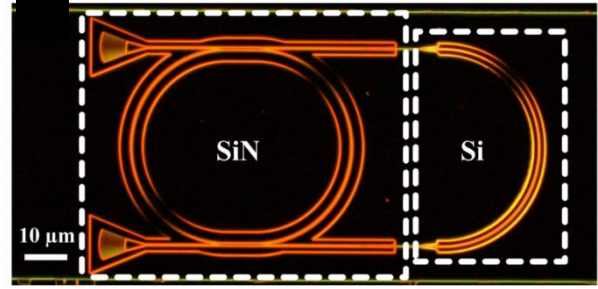


Figure 18. Dark-field optical micrograph image of the fabricated hybrid coupling modulator. The difference in the scattering spectra of Si and SiN results in different color signatures scattered from Si and SiN features.

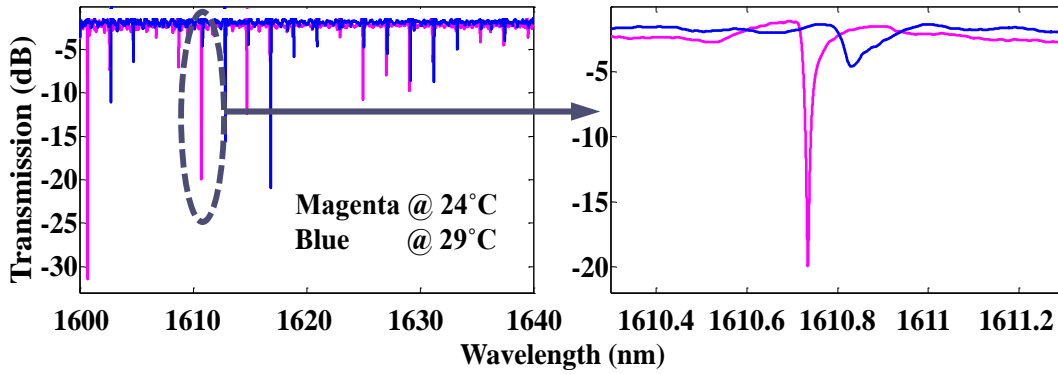


Figure 19. Thermal modulation of the hybrid coupling modulator. At an appropriate bias point at 1610.75 nm , more than 15 dB extinction is recorded. Q_i as high as $200k$ is also measured from the spectrum with finesse of 125 , ~ 9 times larger than the Si device in [12].

Results of DC electro-optical (EO) response of the hybrid modulator shows that the high-speed plasma dispersion is enabled inside the Si waveguide. Unlike thermal EO response, the carrier injection causes a decrease in refractive index, thus a blue shift. The set of devices under-test (DUT's) are measured to have quality factors as high as 2×10^5 after the active functionality is enabled, which shows that with our proposed balanced design of fixed couplers, a 5-fold increase compared to Si device is achievable. On the finesse, which is shown in Eq. 2 to be the main figure of merit, the DUT has record high finesse of 97 , which enables a 7-fold increase compared to SOI modulators. As the proof-of-concept device functionality is established, we are working on the high-speed modulation characterization to finalize this project.

II.D Opto-mechanical devices based on hybrid material platform

II.D.1 Wideband tunable opto-mechanical devices: Among the main components of the integrated coherent optical processing systems are reconfigurable and tunable elements. The main figure of merits for such elements are tuning bandwidth, tuning speed, and power consumption. One of the promising tuning mechanisms with potential to provide excellent performance in all these aspects is opto-mechanical tuning.

The main tuning mechanisms that have been used for the reconfiguration of Si photonic structures to-date are based on: 1) free-carrier dispersion [15,16], the electro-optic effect [17], and the thermo-optic effect [18,19,20,21,22,23,24,25,26]. However, none of these tuning mechanisms provide the required specifications in terms of wide tuning bandwidth, low power consumption, and high reconfiguration speed. While both free-carrier dispersion and electro-optic tuning can potentially provide high tuning speeds, the achievable dynamic range using these techniques are very limited. Furthermore, free carrier tuning suffers from inherent free-carrier loss and its dynamic range is very limited. The application of electro-optic tuning also requires incorporating nonlinear polymers in a Si platform (e.g., a slot-based device). Thermal tuning is the most common technique for the reconfiguration of Si photonic devices as it provides low-loss tuning with moderate dynamic range (e.g., 1- 8 nm). However, the application of thermal tuning also faces major challenges, including slow reconfiguration dynamics (reconfiguration times typically more than 1 μ s), high static power consumption, and thermal cross-talk that limit the integration density of the on-chip photonic structures.

As an alternative technique, mechanical tuning can be used to achieve wideband tuning of photonic devices. While there are a few reports on mechanical tuning of Si photonic structures [27,28,29], this technique has not received much widespread attention.

Figure 21 shows the schematic of the tunable microdisk resonators on the double-layer SOI platform. After patterning the microdisk structure in the double-layer SOI substrate; the thin oxide layer between the two Si layers is partially undercut (see Figure 21(b)). The top and bottom Si layers in such an undercut structure form a capacitor with an air dielectric layer, which allows for the movement of the upper Si layer. Figure 21(c) shows the SEM image of the fabricated structure after undercutting. The tuning of the resonance wavelength is achieved by changing the size of the gap between the two Si layers. An electric voltage is applied between the upper and lower Si layers resulting in an attractive electrostatic force between the two capacitor electrodes that pulls the upper Si layer down and reduces the gap (see Figure 21(c)).

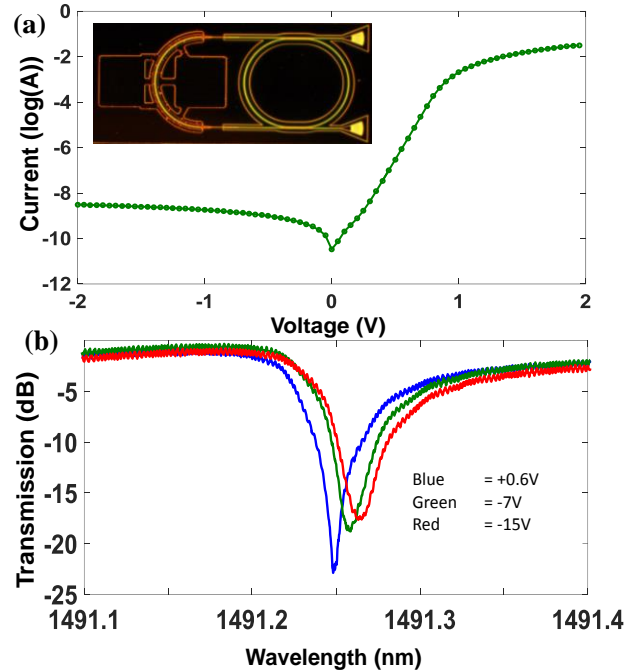


Figure 20. (a) Measured DC i-v curve of the p-n junction diode integrated inside the Si waveguide. The inset shows the micrograph of the fabricated active device with electrical pads. (b) Results of DC characterization of the device. The blue shift of the resonance confirms the free carrier dynamics of the change in effective phase of Si waveguide.

To obtain a high tuning efficiency (defined as the ratio of the wavelength shift ($\Delta\lambda$) to the change in the applied voltage (ΔV), i.e., $\Delta\lambda / \Delta V$), a high sensitivity of the resonance wavelength to the change in the gap size and a relatively strong electrostatic force and/or relatively low structure stiffness for the moving electrode (i.e., the upper Si layer) are required. All of these are achieved by using the structure proposed in this work: the vertical slot architecture with the thin air gap (Figure 21(b)) allows to concurrently achieve wide tuning bandwidth and a low tuning voltage. Furthermore, the upper electrode is patterned to adjust/reduce its stiffness for the target device tuning range.

The proposed opto-mechanical structure supports both TE and TM modes (slot-mode). While the TM mode (i.e., electric field normal to the double SOI wafer surface) of the structure provides slightly higher sensitivity to changes in the gap size, our focus in this work is on the TE mode (i.e., electric field parallel to the double SOI wafer surface) of the structure as it provides lower loss (i.e., higher quality factors for the resonance modes) and allows for more compact resonators with larger free spectral ranges (FSRs). Reducing the gap size results in increasing the resonance wavelength (Figures 21(f) and 21(g), blue curves) of the fundamental TE mode (vertically even mode). While the change in the optical resonance wavelength is almost linearly proportional to the change in the gap size, the change in the gap size is a nonlinear function of the applied voltage and depends on the gap size itself. The maximum tuning range is also limited by the pull-in voltage that limits the maximum change in the gap size. As indicated in Figures 21(f) and 21(g), 35 nm and 22 nm wavelength shifts can be obtained, respectively, for the structures in Figures 21(a) and 21(b) by applying a reasonably small voltage. This shows the unique feature of the proposed structures in providing a very wideband tuning range.

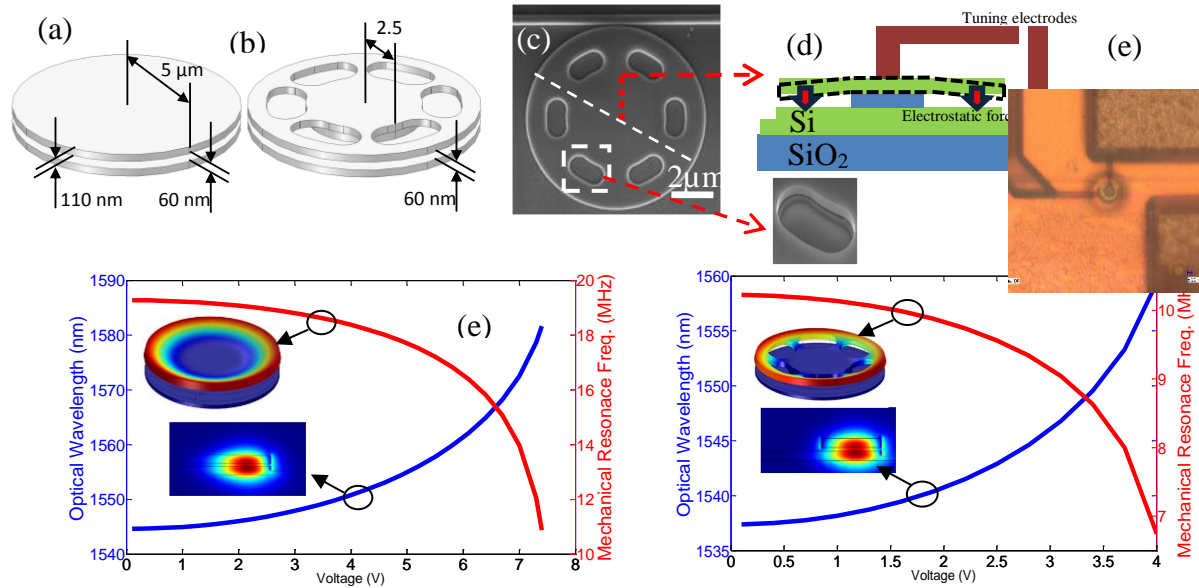


Figure 21. An electrostatically actuated wideband tunable optical resonator: (a), (b) show the schematics of the proposed double-layer resonators. The top and bottom Si layers are both 110 nm thick (including a 50 nm pedestal for the bottom layer) with an initial gap of 60 nm; (c) SEM image of the proposed opto-mechanical structure; (d) the cross section view of the microdisk cavity and the location of the tuning electrodes; (e) microscope image of the fabricated device; (f), (g): variation of the optical wavelength (blue curve, left axis) and the resonance frequency of the 1st mechanical floppy mode (red curve, right axis) as a function of the applied voltage between the two Si layers in the two structures shown in (a) and (b), respectively. The scaling in (a) and (b) is selected to clearly show different dimensions.

The tuning speed of the proposed electrostatically tunable device is limited by the mechanical time constant of the moving electrode, which is in-turn limited by its fundamental mechanical resonance frequency (f_{mech}). The patterned and unpatterned structures exhibit a range of f_{mech} depending on the applied voltage starting at 19 MHz and 10 MHz (corresponding to the rise times, t_r , of 19 ns and 35 ns), respectively, for structures in Figures 21(a) and 21(b) (see Figures 21(e) and 21(f), red curves). One way to increase f_{mech} is to extend the radius of the anchor. For example, simulations show $f_{\text{mech}} > 50$ MHz (i.e., $t_r = 7$ ns) when the radii of the anchor and the upper unpatterned disk are 3.5 μm and 5 μm , respectively; and the thickness of the upper and lower Si layers are both 110 nm. This mechanical resonance frequency can result in a switching time constant of a few nanoseconds for the optical device. However, increasing the mechanical resonance frequency in this structure comes at the cost of losing the tuning efficiency ($\Delta\lambda / \Delta V$), which in turn can limit the tuning bandwidth for a given operating voltage. This trade-off among the tuning range, the operation voltage, and the tuning speed can be used to design devices for any desired application by adjusting the stiffness of the upper electrode through tailoring its geometry and pattern.

II.E Wideband coherent comb and soliton generation

Optical frequency comb generation has attracted a lot of interest in the past few years [30,31,32,33,34,35,36,37,38]. Previously we reported that we have developed a simulation platform for the modeling of nonlinear pulse evolution in integrated photonic resonators and waveguides. Following up on our initial results, using this tool we have studied frequency comb generation and soliton formation in high-Q resonators and have developed a rigorous formulation and complete understanding of the effect of phase modulation on the dynamics of the combs. Our numerical simulations of the governing equation suggest that input phase modulation provides a deterministic path, without having to walk the system through a chaotic phase by a tailored pump wavelength sweeping ramp [39,40], towards soliton formation in WGM resonators. Additionally, we have studied the effect of the modulation in the presence of third- and fourth-order dispersion and have verified that this technique works just fine even in the presence of higher-order dispersion coefficients. We have also used phase modulation for the manipulation of pulses and have shown that it enhances the stability of the generated pulse in a micro-resonator [41,42,43]. Finally, we have shown that the input modulation can be turned off adiabatically without affecting the generated solitons. Combined with optoelectronic modulators, input phase modulation introduces a viable approach towards making the advantages of temporal solitons available at small footprints. Our findings are summarized in Ref. [44].

It is worth noting that phase modulation has been used in the context of diffractive and fiber cavities to move pulses, form pulse arrays, and suppress the interaction of solitons in fibers [45,46,47,48]. In such studies, a “holding” or “driving beam” is used to balance the cavity dissipation, and a pulsed laser is used to inject a pulse (e.g., a Gaussian pulse) into the cavity. This pulse, upon propagation in the resonator, evolves into a soliton (see, e.g., [49]). A phase modulated “addressing beam” is then used to move the pulse over the holding beam. We note that the phase-modulation-induced sidebands correspond to a modulation added to the CW background in the intra-cavity field, which can grow into a soliton when it is strong enough to overcome the resonator losses. Thus, with phase modulation, solitons can be formed without going through an unstable state and without an injected pulse in a micro-resonator.

Our simulations are based on the following damped, driven, nonlinear Schrodinger equation

$$(3) \quad \frac{\partial y}{\partial t} = - (1 + ia)y - i \frac{b}{2} \frac{\partial^2 y}{\partial q^2} + i|y|^2 y + F_0 \exp[id_M \sin q].$$

Here, $y(q, t)$ is the total intra-cavity field envelope, a is the normalized detuning, b is the normalized second-order dispersion coefficient, F_0 is proportional to the input power, and d_M is the modulation depth. The spatial coordinate q is the azimuthal angle around the resonator and t is the evolution time normalized to the photo lifetime of the cavity. The split-step Fourier algorithm [50] has been used for our numerical simulations of the Schrodinger equation. The simulations reported here have been performed for a calcium fluoride (CaF_2) resonator of radius $r = 2.5\text{mm}$. We have also performed similar simulations for silicon nitride (Si_3N_4) micro-resonators of radius in the range $100\text{-}900\mu\text{m}$. A schematic of the system we study is depicted in Figure 22.

Figure 23 illustrates the generation of a soliton starting from a cold cavity when the pump phase is modulated at a depth corresponding to the transfer of $\sim 12\%$ of the pump power to the primary sidebands ($d_M = 0.65$). As seen in the left panel in Figure 23(a), a stable sharply peaked soliton is generated at $q = \pi/2$. The spectrum of the pulse is smooth and broadband (Figure 23(a), middle panel) and the time evolution of the phases of the comb lines (right panel) clearly illustrates phase locking, i.e., the establishment of a fixed relationship between the phases of different comb lines, after the soliton is formed. The waveform and frequency spectrum of this pulse (Figure 23

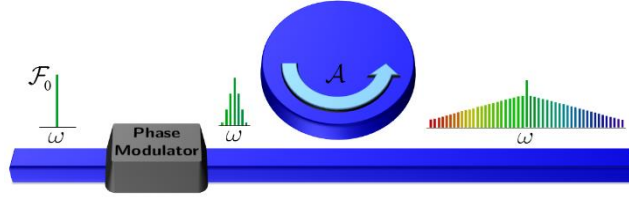


Figure 22. Schematic of the structure under study. A waveguide is side-coupled to a resonator. The phase of the input laser is modulated before it couples into the resonator. The modulation leads to the generation of sidebands which seed the comb generation process. The equipment for stabilizing the pump-resonance detuning is not shown here.

(b), (c), respectively) are essentially identical to those of a soliton generated from a Gaussian pulse as the initial condition. It suggests that parametric seeding by input phase modulation has walked the system towards the same fixed point as that achieved by a particular initial condition. In Figure 23(d), a closer look is cast upon the spectra of the pulses generated in the two scenarios in the vicinity of the pumped resonance. The spectrum of the soliton produced by phase modulation (blue curve) and that of the soliton evolved from a suitable non-constant initial condition (red spikes) differ only in the few modal fields close to the pump (taller central spike) and are identical otherwise. The difference between the total field envelopes is much harder to see, such that if we overlay the corresponding curves on top of each other in one figure, they are virtually the same.

Results presented in Figure 23 assume that the resonator has zero energy at the onset of the input phase modulation. In an experimental setup, however, the precise synchrony of the pump turn-on time and that of the phase modulator might be difficult. To account for this effect, we have shown in Figure 21(a) the evolution of the intra-cavity field when the phase modulation is applied to a resonator initially at equilibrium. The equilibrium value of the intra-cavity field y_e can be found from the Schrodinger equation by setting all the derivatives equal to zero [51]. As seen in the left panel of Figure 21(a), in this case a number of pulses are generated in the resonator. The initial number of pulses depends on the total energy inside the resonator when the modulation is turned on [52]. In the presence of pump phase modulation, each pulse is forced to move towards

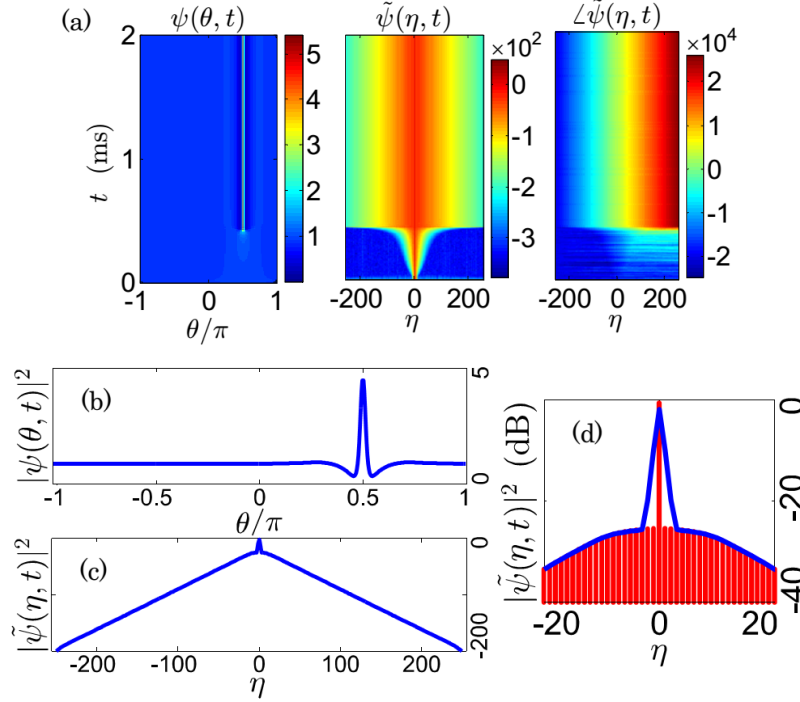


Figure 23. (a) The temporal evolution of the waveform ($|\psi|$, left), spectrum ($|\tilde{\psi}|$, middle), and phase ($\angle \tilde{\psi}$, right) of the intra-cavity field starting from zero initial conditions and with input phase modulation. The phase has been unwrapped. ($\alpha = 2$, $F = 1.4103$, $\delta_M = 0.65$) (b) The generated pulse corresponding to $t = 2$ ms in (a). (c) The spectrum (in dB) of the pulse corresponding to $t = 2$ ms in (a). (d) Comparison of the spectrum near the pump for the generated soliton in (a) (blue curve) and a soliton evolved from a weak Gaussian pulse, $\psi(q, 0) = 0.4 + 0.2 \exp[-q^2 / 2(0.1)^2]$ as the initial condition (red spikes).

$q = \pi/2$ and merge with the other pulses. The pulse generated at $q = -\pi/2$ appears first to be stable but that too starts to move towards $q = \pi/2$ after $t = 2$ ms. All of the pulses eventually merge, leaving one stable pulse whose waveform and spectrum are the same as those depicted, respectively, in Figs. 20(b) and (c). These observations suggest that $q = \pm\pi/2$ are fixed points; $q = \pi/2$ is stable while $q = -\pi/2$ is unstable.

The behavior observed in Figures 23 and 24 can be understood by considering the intra-cavity field momentum [53]. We have shown that in the presences of phase modulation, there will be two equilibria in the cavity at the positions of the extrema of the modulation phase profile, i.e. the exponent in the driving field in the Schrodinger equation. The pulses inside a cavity will be dragged towards the maxima of the modulation profile by a force proportional with the modulation depth. The analysis based on the pulse momentum also shows that, small perturbations can destabilize a pulse centered at $q = -\pi/2$ and move it away from this point; any pulse inside the resonator will be dragged towards $q = \pi/2$. In other words, $q = \pi/2$ is stable while $q = -\pi/2$ is unstable. To further test this explanation, we show in Figure 21(b) an example where the initial condition in the absence of phase modulation is a weak Gaussian pulse centered at a point slightly to the right of $q = -\pi/2$. This pulse evolves rapidly into a soliton. The modulation is turned on at $t = 1$ ms which results in the deflection of the soliton towards $q = \pi/2$. The soliton propagates without deviating to either side after reaching this point. The preceding discussion also shows that solitons generated through input phase modulation tend to be more robust than solitons in the absence of this type of seeding, because any perturbation in the position of the pulse will be opposed and suppressed by the modulated pump. We note that a non-zero phase for the modulator will shift the

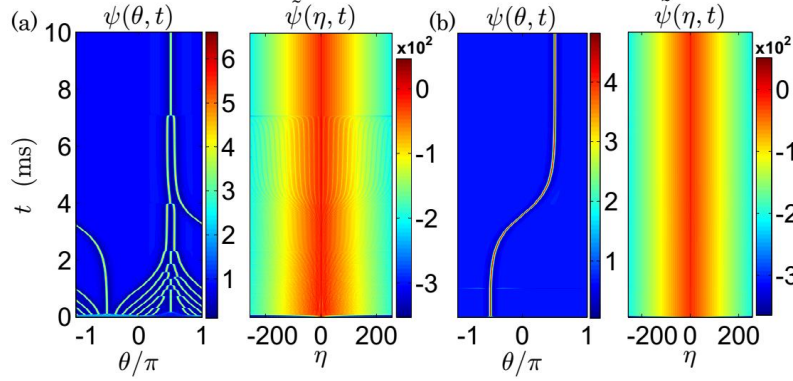


Figure 24. (a) Temporal evolution of the waveform (left) and spectrum (right) of the field envelope starting from $|y(q, 0)|^2 = 0.9$ and with pump phase modulation. All parameters are the same as those in Figure 20(a). (b) Same as (a) except starting with a weak Gaussian pulse $y(q, 0) = 0.2 + \exp[-(q + 0.49p)^2 / 2(0.1)^2]$ and no modulation. The modulation is turned on at $t = 1$ ms. The vertical axis is time, as that in (a). ($\alpha = 2$, $F_0 = 1.3722$, $\delta_M = 0.65$)

equilibria and consequently the pulse position. We have performed the same set of simulations in Si_3N_4 ring resonators with sub-million quality factors and have observed the same results even in the presence of third-order dispersion. Parallel efforts on the fabrication of high-Q silicon nitride resonators in our group suggest that the required quality factors are within reach in this platform.

III. Publications and Presentations

III.A Journal papers

- [1] P. Alipour, A. A. Eftekhar, A. H. Atabaki, and A. Adibi, "A thermally reconfigurable reflection canceller for adaptive on-chip optical isolation on SOI," *Optics Letters* 39, pp. 1141-1144, (2014).
- [2] M. Miri, M. Sodagar, K. Mehrany, A. A. Eftekhar, A. Adibi, B. Rashidian, "Design and Fabrication of Photonic Crystal Nano-Beam Resonator: Transmission Line Model," *Journal of Lightwave Technology* 32, pp. 91-98, (2014)
- [3] M. Sodagar, R. Pourabolghasem, A. A. Eftekhar, and A. Adibi, "High-efficiency and wideband interlayer grating couplers in multilayer Si/SiO₂/SiN platform for 3D integration of optical functionalities," *Optics Express* 22, pp. 16767-16777, (2014).
- [4] M. Sodagar, A. H. Hosseinnia, A. A. Eftekhar, A. Adibi, "Field-programmable optical devices based on resonance elimination," *Optics Letters* 39, pp. 4545-4549, (2014).
- [5] M. Sodagar, M. Miri, A. A. Eftekhar, A. Adibi, "Optical bistability in a one-dimensional photonic crystal resonator using a reverse-biased pn-junction," *Optics Express* 3, pp. 2676-2685, (2015).
- [6] H. Moradinejad, A. H. Atabaki, A. H. Hosseinnia, A. A. Eftekhar, and A. Adibi, "Double-layer crystalline silicon on insulator material platform for integrated photonic applications," *IEEE Photonics Journal* 7, pp. 1-8 (2014).
- [7] H. Taheri, A. A. Eftekhar, K. Wiesenfeld, and A. Adibi, "Soliton formation in whispering-gallery-mode resonators via input phase modulation," *IEEE Photonics Journal* 7, pp. 1-9 (2015).
- [8] H. Taghinejad, M. Taghinejad, A. Tarasov, M.-Y. Tsai, A. H. Hosseinnia, H. Moradinejad, P. M. Campbell, A. A. Eftekhar, E. M. Vogel and A. Adibi, Resonant Light-Induced Heating in Hybrid Cavity-Coupled 2D Transition Metal Dichalcogenides, *ACS Photonics* (2016).
- [9] H. Taheri, P. Del'Haye, A. A. Eftekhar, K. Wiesenfeld and A. Adibi, Self-synchronization

of Kerr-nonlinear Optical Parametric Oscillators, arXiv preprint arXiv:1602.08523 (2016).

[10] A. H. Hosseinnia, A. H. Atabaki, A. A. Eftekhar, and A. Adibi, "A high-quality silicon on silicon nitride integrated optical platform with an octave-spanning adiabatic interlayer coupler," *Opt. Express* 23, 30297-30307 (2015)

[11] M. Sodagar, A.H. Hosseinnia, P. Isautier, H. Moradinejad, S. Ralph, A.A. Eftekhar, and A. Adibi, "Compact, 15 Gb/s electro-optic modulator through carrier accumulation in a hybrid Si/SiO₂/Si microdisk," *Opt. Express* 23, 28306-28315 (2015).AA

[12] H. Taghinejad, M., A. Tarasov, MY Tsai, AH, Hosseinnia, H Moradinejad, PM Campbell, AA Eftekhar, EM Vogel, A Adibi,"Resonant Light-Induced Heating in Hybrid Cavity-Coupled 2D Transition-Metal Dichalcogenides," *ACS Photonics* 3, 700-707 (2016).

[13] R. Dehghannasiri, A.A. Eftekhar, and A. Adibi, "High-speed optomechanically-tunable photonic devices on double-layer SOI platforms," In preparation.

III.B Conference presentations

[14] R. Dehghannasiri, A. A. Eftekhar and A. Adibi, Raman-Like Stimulated Brillouin Scattering in SiN Waveguides, presented at the CLEO: Science and Innovations, 2016, pp. SM1E. 8.

[15] T. Fan, A. Eftekhar, H. Taghinejad, P. Ajayan and A. Adibi, Optical Properties of MoS₂/MoSe₂ Heterostructures, presented at the Laser Science, 2016, pp. JTh2A. 99.

[16] A. H. Hosseinnia, H. Moradinejad, M. Sodagar, A. A. Eftekhar and A. Adibi, Hybrid CMOS-compatible Material and Device Platform for Integrated Nanophotonics, presented at the CLEO: Science and Innovations, 2016, pp. SM4G. 1.

[17] H. S. Mousavi, H. Taheri, A. H. Hosseinnia, A. A. Eftekhar and A. Adibi, Large Enhancement of Second Harmonic Emission Using Lattice Plasmon Polaritons, presented at the CLEO: QELS_Fundamental Science, 2016, pp. FW4A. 3.

[18] S. H. S. Mousavi, H. Taghinejad, M. Taghinejad, A. A. Eftekhar and A. Adibi, Strong light-matter interaction through mode engineering in plasmonic nanoantenna arrays, presented at the Progress in Electromagnetic Research Symposium (PIERS), 2016, pp. 1127-1127.

[19] H. Taghinejad, M. Taghinejad, A. Tarasov, M.-Y. Tsai, A. H. Hosseinnia, H. Moradinejad, P. M. Campbell, A. A. Eftekhar, E. M. Vogel and A. Adibi, Resonant Light-Induced Heating in Hybrid Cavity-Coupled 2D Transition-Metal Dichalcogenides, *ACS Photonics* 3 (4), 700-707 (2016).

[20] H. Taheri, P. Del'Haye, A. A. Eftekhar, K. Wiesenfeld and A. Adibi, Self-synchronization and Phase Steps in Microresonator-based Optical Frequency Combs, presented at the CLEO: Science and Innovations, 2016, pp. STu1H. 6.

[21] H. Moradinejad, A. H. Atabaki, H. Taheri, A. A. Eftekhar, and A. Adibi, "Polarization Cross-coupling Between Microring and Bus Waveguide in Double-layer SOI." *CLEO: Science and Innovations*, (2014).

[22] M. Sodagar, A. H. Hosseinnia, A. A. Eftekhar, and A. Adibi, "Multilayer Platform for Low-Power/Passive Configurable Photonic Device," *CLEO: Science and Innovations*, (2014).

[23] R. Dehghannasiri, A. A. Eftekhar, M. Sodagar, and A. Adibi, "Wideband-Tunable Optical Resonators on Double-Layer SOI Platforms using Electrostatic Actuation," *CLEO: Science and Innovations*, (2014).

[24] M. Sodagar, H. Moradinejad, A. A. Eftekhar, and A. Adibi. "Electro-optic Modulation of Small Disk Microcavity through Gated Graphene," *CLEO: Science and Innovations*, (2014).

[25] M. Sodagar, R. Pourabolghasem, A. A. Eftekhar, and Ali Adibi, "Interlayer Grating Coupler

for Si/SiO₂/SiN platform,” IEEE Photonic Conference, (2014).

[26] M. Sodagar, A. H. Hosseinnia, A. A. Eftekhar, and A. Adibi, “Integrated Field-programmable 2 by 2 Optical Switch on a Multilayer Platform,” IEEE Photonics Conference, (2014).

[27] H. Taheri, A. A. Eftekhar, A. Adibi, “Frequency Comb Generation Threshold Reduction and Soliton Formation via Input Phase Modulation,” IEEE Photonics Conference, (2014).

[28] H. Taheri, A. A. Eftekhar, A. Adibi, “Pulse Formation via Parametric Seeding in Whispering Gallery-Mode Microresonators with Kerr Nonlinearity,” Frontiers in Optics, (2014)

[29] A. H. Hosseinnia, H. Maoradinejad, M. Sodagar, Q. Li, A. H. Atabaki, , A. A. Eftekhar, and Ali Adibi, “A Novel CMOS-compatible Hybrid Material and Device Platform for Reconfigurable Integrated Nanophotonics,” International Conference and Exhibition on Lasers, Optics & Photonics (2014) *Invited talk*.

[30] A. Adibi, “A Novel CMOS-compatible Hybrid Material Platform for Integrated Nanophotonics,” The 3rd Global Conference on Materials Science and Engineering (CMSE), (2014) *Keynote speech*.

IV. References:

- [1] B. Jalali, and S. Fathpour. "Silicon photonics," J. of Lightwave Tech., vol. 24, no. 12, 4600-4615 (2006).
- [2] D. Moss *et al.* "New CMOS-compatible platforms based on silicon nitride and Hydex for nonlinear optics" Nat. Photonics 7, 597–607 (2013).
- [3] A. Gondarenko, *et al* "High confinement micron-scale silicon nitride high Q ring resonator." Opt. Express 17, 11366–70 (2009).
- [4] Q. Li *et al* "Vertical integration of high-Q silicon nitride micro-resonators into silicon-on-insulator platform." Opt. express 21, no. 15 18236-18248 (2013).
- [5] M. Sodagar, R. Pourabolghasem, A. A. Eftekhar, and A. Adibi, "High-efficiency and wideband interlayer grating couplers in multilayer Si/SiO₂/SiN platform for 3D integration of optical functionalities," Optics Express, 22, pp. 16767-16777, (2014).
- [6] J. Bauters, M. Davenport, M. Heck, J. K. Doylend, A. Chen, A. W. Fang, and J. E. Bowers. "Silicon on ultra-low-loss waveguide photonic integration platform." Optics express 21, no. 1 (2013): 544-555.
- [7] H. Moradinejad, *et al* "Double-layer crystalline silicon on insulator material platform for integrated photonic applications." IEEE Photonics Journal, vol. 6, no.6 (2014).
- [8] E. Timurdogan, C. Agaskar, J. Sun, E. Hosseini, A. Biberman, and M. Watts, "An ultralow power athermal silicon modulator." Nat. Commun. 5, 4008 (2014).
- [9] M. Sodagar, A. H. Hosseinnia, P. Isautier, H. Moradinejad, S. Ralph, A. A. Eftekhar, and A. Adibi. "Compact, 15 Gb/s electro-optic modulator through carrier accumulation in a hybrid Si/SiO₂/Si microdisk." Opt. Express 23(22), 28306–28315 (2015).
- [10] C. Sun, et al. "Single-chip microprocessor that communicates directly using light." Nature 528(7583) 534-538 (2015).
- [11] M. Popović, "Resonant optical modulators beyond conventional energy-efficiency and modulation frequency limitations." IPR, IMC2 (2010).
- [12] W. Sacher, W. M. J. Green, S. Assefa, T. Barwicz, H. Pan, S. M. Shank, Y. A. Vlasov, and J. K. S. Poon. "Coupling modulation of microrings at rates beyond the linewidth limit." Opt. express 21(8), 9722–9733 (2013).
- [13] G. Cocorullo, F. G. Della Corte, and I. Rendina. "Temperature dependence of the thermo-optic coefficient in crystalline silicon between room temperature and 550 K at the wavelength of 1523 nm." Applied physics letters 74(22), 3338–3340 (1999).
- [14] A. Arbabi, and L. L. Goddard. "Measurements of the refractive indices and thermo-optic coefficients of SiN and SiO₂ using microring resonances." Opt. letters 38(19), 3878–3881 (2013).
- [15] H. Lira, S. Manipatruni, and M. Lipson, "Broadband hitless silicon electro-optic switch for on-chip optical networks," Opt. Express 17, 22271–22280 (2009).
- [16] C. Li, L. Zhou, and A. Poon, "Silicon microring carrier-injection-based modulators/switches with tunable extinction ratios and OR-logic switching by using waveguide cross-coupling," Optics Express 15, 5069–5076 (2007).
- [17] J. Takayesu, M. Hochberg, T. Baehr-Jones, E. Chan, G. Wang, P. Sullivan, Y. Liao, J. Davies, L. Dalton, A. Scherer et al., "A Hybrid Electrooptic Microring Resonator- Based 1x 4 ROADM for Wafer Scale Optical Interconnects," J. Lightwave Tech. 27, 440–448 (2009).
- [18] M. S. Rasras, D. M. Gill, S. S. Patel, K.-Y. Tu, Y.-K. Chen, A. E. White, A. T. S. Pomerene, D. N. Carothers, M. J. Grove, D. K. Sparacin, J. Michel, M. A. Beals, and L. C. Kimerling,

- “Demonstration of a fourth-order pole-zero optical filter integrated using CMOS processes,” *JOURNAL OF LIGHTWAVE TECHNOLOGY* **25**, 87–92 (2007).
- [19] X. Wang, J. A. Martinez, M. S. Nawrocka, and R. R. Panepucci, “Compact thermally tunable silicon wavelength switch: Modeling and characterization,” *IEEE Phot. Tech. Lett.* **20**, 936–938 (2008).
- [20] H.-Y. Ng, M. R. Wang, D. Li, X. Wang, J. Martinez, R. R. Panepucci, and K. Pathak, “1x4 wavelength reconfigurable photonic switch using thermally tuned microring resonators fabricated on silicon substrate,” *IEEE Phot. Tech. Lett.* **19**, 704–706 (2007).
- [21] I. Kiyat, A. Aydinli, and N. Dagli, “Low-power thermo-optical tuning of SOI resonator switch,” *IEEE Phot. Tech. Lett.* **18**, 364–366 (2006).
- [22] T. Chu, H. Yamada, S. Ishida, and Y. Arakawa, “Compact 1 x N thermo-optic switches based on silicon photonic wire waveguides,” *Opt. Exp.* **13**, 10109–10114 (2005).
- [23] D. Geuzebroek, E. Klein, H. Kelderman, N. Baker, and A. Driessen, “Compact wavelength-selective switch for gigabit filtering in access networks,” *IEEE Phot. Tech. Lett.* **17**, 336–338 (2005).
- [24] T. Goh, M. Yasu, K. Hattori, A. Himeno, M. Okuno, and Y. Ohmori, “Low loss and high extinction ratio strictly nonblocking 16 x 16 thermo-optic matrix switch on 6-in wafer using silica-based planar lightwave circuit technology,” *J. light. Wave. Tech.* **19**, 371–379 (2001).
- [25] R. Jones, J. Doyle, P. Ebrahimi, S. Ayotte, O. Raday, and O. Cohen, “Silicon photonic tunable optical dispersion compensator,” *OPTICS EXPRESS* **15**, 15836–15841 (2007).
- [26] F. Horst, R. Germann, U. Bapst, D. Wiesmann, B. Offrein, and G. Bona, “Compact tunable FIR dispersion compensator in SiON technology,” *IEEE Phot. Tech. Lett.* **15**, 1570–1572 (2003).
- [27] Eichenfield, Matt, Ryan Camacho, Jasper Chan, Kerry J. Vahala, and Oskar Painter. “A picogram-and nanometre-scale photonic-crystal optomechanical cavity.” *Nature* **459**, no. 7246, 550–555 (2009).
- [28] Deotare, Parag B., Murray W. McCutcheon, Ian W. Frank, Mughees Khan, and Marko Loncar. “Coupled photonic crystal nanobeam cavities,” *Applied Physics Letters* **95**, no. 3 031102–031102 (2009).
- [29] Wiederhecker, Gustavo S., Long Chen, Alexander Gondarenko, and Michal Lipson. “Controlling photonic structures using optical forces,” *Nature* **462**, no. 7273: 633–636 (2009).
- [30] T. J. Kippenberg, R. Holzwarth, and S. A. Diddams, “Microresonator-based optical frequency combs,” *Science* vol. 332, pp. 555–559, 2011.
- [31] Y. K. Chembo, N. Yu, “Modal expansion approach to optical-frequency-comb generation with monolithic whispering-gallery-mode resonators,” *Physical Review A* vol. 82, 033801, 2010.
- [32] A. B. Matsko, A. A. Savchenkov, W. Liang, V. S. Ilchenko, D. Seidel, and L. Maleki, “Whispering gallery mode oscillators and optical comb generators,” *Proc. of 7th Symp. Frequency Standards and Metrology*, 1, 539, 2009.
- [33] A. B. Matsko, A. A. Savchenkov, W. Liang, V. S. Ilchenko, D. Seidel, and L. Maleki, “Mode-locked Kerr frequency combs,” *Optics Letters* vol. 36, pp. 2845–2847, 2011.
- [34] S. Coen, H. G. Randle, T. Sylvestre, and M. Erkintalo, “Modeling of octave-spanning Kerr frequency combs using a generalized mean-field Lugiato–Lefever model,” *Optics Letters* vol. 38, pp. 37–39, 2013.
- [35] Y. K. Chembo, C. R. Menyuk, “Spatiotemporal Lugiato–Lefever formalism for Kerr-comb generation in whispering-gallery-mode resonators,” *Physical Review A* **87**, 053852, 2013.

- [36] I. V. Barashenkov, M. M. Bogdan, and V. I. Korobov, "Stability diagram of the phase-locked solitons in the parametrically driven, damped nonlinear Schrödinger equation," *Europhysics Letters* vol. 15.2, 113, 1991.
- [37] T. Hansson, T. Hansson, D. Modotto, and S. Wabnitz, "On the numerical simulation of Kerr frequency combs using coupled mode equations," *Optics Comm.* vol. 312, 134, 2014.
- [38] T. Herr, V. Brasch, J. D. Jost, C. Y. Wang, N. M. Kondratiev, M. L. Gorodetsky, and T. J. Kippenberg, "Temporal solitons in optical microresonators," *Nature Photonics* vol. 8.2, 145, 2014.
- [39] S. Coen, and M. Erkintalo, "Universal scaling laws of Kerr frequency combs," *Optics Letters* vol. 38, 1790 (2013).
- [40] M. Lamont, Y. Okawachi, and A. L. Gaeta, "Route to stabilized ultrabroadband microresonator-based frequency combs," *Optics Letters* vol. 38.18, 3478, 2013.
- [41] A. A. Savchenkov, A. B. Matsko, V. S. Ilchenko, I. Solomantine, D. Seidel, and L. Maleki, "Tunable optical frequency comb with a crystalline whispering gallery mode resonator," *Phys. Rev. Lett.* vol. 101, 093902, 2008.
- [42] D. V. Strekalov, and N. Yu, "Generation of optical combs in a whispering gallery mode resonator from a bichromatic pump," *Phys. Rev. A* vol. 79, 041805, 2009.
- [43] S. B. Papp, P. Del'Haye, and S. A. Diddams, "Parametric seeding of a microresonator optical frequency comb," *Optics Express* vol. 21.15, 17615, 2013.
- [44] H. Taheri, A. A. Eftekhar, K. Wiesenfeld, and A. Adibi, "Soliton formation in whispering-gallery-mode resonators via input phase modulation," *IEEE Photonics Journal* 7, pp. 1-9 (2015).
- [45] N. Akhmediev, and A. Ankiewicz, *Dissipative Solitons* vol. 661, Lecture Notes in Physics, Springer, 2005, Chap. 4.
- [46] G. S. McDonald, and W. J. Firth, "Spatial solitary-wave optical memory," *JOSA B* vol. 7, 1328-1335, 1990.
- [47] S. Wabnitz, "Suppression of interactions in a phase-locked soliton optical memory," *Optics Lett.* 18, 601-603, 1993.
- [48] J. K. Jang, M. Erkintalo, S. G. Murdoch, and S. Coen, "Transient Dynamics of Cavity Soliton Merging," *Advanced Photonics Congress*, paper JTU6A.7 (Optical Society of America, 2014).
- [49] F. Leo, S. Coen, P. Kockaert, S.-P. Gorza, Ph. Emplit, and M. Haelterman, "Temporal cavity solitons in one dimensional Kerr media as bits in an all-optical buffer," *Nature Photonics* vol. 4, 471-476, 2010.
- [50] F. D. Tappert and R. H. Hardin, "Applications of the split-step Fourier method to the numerical solution of nonlinear and variable coefficient wave equations," *SIAM Rev.* 5, 423, 1973.
- [51] C. Godey, I. V. Balakireva, A. Coillet, and Y. K. Chembo, "Stability analysis of the spatiotemporal Lugiato-Lefever model for Kerr optical frequency combs in the anomalous and normal dispersion regimes," *Physical Rev. A* 89, 063814, 2014.
- [52] A. B. Grudinin, D. J. Richardson, and D. N. Payne, "Energy quantization in figure eight fiber laser," *Electronics Lett.* 28.1, 67, 1992.
- [53] E. V. Zemlyanaya, and I. V. Barashenkov, "Traveling solitons in the damped-driven nonlinear Schrödinger equation," *SIAM Journal on Applied Mathematics*, 64, 800-818, 2004.